Semiconducting photosensitizer-incorporated copolymers as near-infrared afterglow nanoagents for tumor imaging

Cui, Dong; Xie, Chen; Li, Jingchao; Lyu, Yan; Pu, Kanyi

2018

Cui, D., Xie, C., Li, J., Lyu, Y., & Pu, K. (2018). Semiconducting photosensitizer-incorporated copolymers as near-infrared afterglow nanoagents for tumor imaging. Advanced healthcare materials, 7(18), 1800329-. doi:10.1002/adhm.201800329

https://hdl.handle.net/10356/137158

https://doi.org/10.1002/adhm.201800329

WILEY-VCH

DOI: 10.1002/((please add manuscript number))
Article type: Article

Invited Submission

Semiconducting Photosensitizer-incorporated Copolymers as Near-Infrared Afterglow Nanoagents for Tumor Imaging

*Dong Cui, Chen Xie, Jingchao Li, Yan Lyu and Kanyi Pu**

D. Cui, Dr. C. Xie, Dr. J. Li, Y. Lyu, Prof. K. Pu
School of Chemical and Biomedical Engineering, Nanyang Technological University, Singapore 637457, Singapore
E-mail: kypu@ntu.edu.sg

Keywords: polymer nanoparticles, optical imaging, tumor imaging, near-infrared fluorescence, afterglow imaging

Abstract. The fact that cancer metastasis is the main cause of death for most cancer patients necessitates the development of imaging tools for sensitive detection of metastases. Although optical imaging has high temporospatial resolution, tissue autofluorescence compromises the sensitivity for *in vivo* imaging of cancer metastasis. We herein report the synthesis of a series of photosensitizer-incorporated poly(*p*-phenylenevinylene) (PPV)-based semiconducting copolymers and their utility as near-infrared (NIR) afterglow imaging nanoagents that emit light after cessation of light irradiation. As compared with non-doped nanoparticles, the nanoparticles derived from the photosensitizer-incorporated copolymers have red-shifted NIR luminescence and amplified afterglow signals, allowing it to detect tiny peritoneal metastatic tumors almost invisible to naked eye. Moreover, the intrinsically oxygen-sensitive nature of afterglow makes those nanoagents potentially useful for *in vivo* imaging of oxygen levels. Thus, this study introduces a generation of light-excitation-free background-minimized optical imaging agents for sensitive detection of disease tissues *in vivo*.

1. Introduction

Cancer metastasis with its complex cell-biological mechanism, systemic nature and drug resistance is the main cause of recurrence and death for most cancer patients.[1] Early diagnosis of metastases thus plays a critical role in effective treatment of cancer. Radiologic imaging approaches such as magnetic resonance imaging (MRI), computed tomography (CT), ultrasound and positron emission tomography (PET) have been used for diagnosis of tumor metastases.[2] For examples, the combination of multiple imaging (CT/PET) have been explored for detection of tumor metastasis in lymph nodes,[3] and MRI in association with pH-responsive nanoparticles as contrast agents has been used for detection of liver metastasis.[4] However, because of limited resolution for PET and the high potential of false positive signal for MRI, current methods relatively have low specificity and sensitivity.[5]

In comparison with those clinical imaging modalities, optical imaging has high temporospatial resolution, and thus holds great potential for early diagnosis of cancer metastasis. Optical imaging agents such as organic dyes,[6] quantum dots,[7] graphene oxide,[8] inorganic nanoparticles[9] and polymeric nanoprobes[10] have been developed for detection of tumor metastases. However, because these agents rely on fluorescence that requires real-time light excitation, they suffer from high tissue autofluorescence, leading to compromised sensitivity.[11]

As an emerging molecular optical imaging method, afterglow or persistent luminescence has drawn more and more attention for its low background and high sensitivity as a result of eliminated real-time light excitation.[12] However, only a few kinds of inorganic nanoparticles doped with rare-earth metals or heavy metals (such as europium, praseodymium and chromium) have the ability to emit afterglow,[13] and they have been tested for tumor imaging,[13a] vascular imaging,[14] *in vivo* cell tracking,[13b] and cell targeting.[15] However, these inorganic afterglow nanoparticles have not been exploited for imaging of metastatic tumor tissues in living mice.[16]

Semiconducting polymer nanoparticles (SPNs) have been proved as a new category of optical agents for molecular imaging (including fluorescence,[17] chemiluminescent[18] and photoacoustic imaging[19]) and phototherapy (including photodynamic[20] and photothermal therapy[21]). The biological applications of SPNs range from tumor imaging,[22] to evolution of drug-induced toxicity,[23] monitoring of physiological indexes and biomarkers[24] and to photothermal activation of gene expression[25] and protein-ion channels.[26] Recently, we discovered that poly(phenylenevinylene) (PPV)-based SPNs could emit afterglow luminescence after removal of light excitation.[27] However, because these PPVs can only emit visible light, physical doping of a near-infrared dye into the nanoparticles is required to shift the emission to the ideal NIR window with reduced light scattering. This complicated the nanoparticle synthesis and led to relatively large size (~35 nm).

We herein report the design and synthesis of poly(p-phenylenevinylene)s (PPVs) incorporated with a NIR photosensitizer for *in vivo* afterglow imaging of metastatic tumors in living mice. Tetraphenylporphyrin (TPP) is used as the NIR photosensitizer and copolymerized into the polymers, leading to red-shifted emission and relatively small size (~ 25 nm). Moreover, because the afterglow intensity is determined by the amount of high-energy intermediate (PPV-dioxetane) generated from the π^2-π^2 cycloaddition reaction between the vinylene bonds and single oxygen ($^1O_2$) [27] incorporation of TPP promotes $^1O_2$ generation and thus amplifies afterglow. In the following, we describe the synthesis of TPP-incorporated PPVs and the preparation of related water-soluble nanoparticles, followed by analysis of their optical and afterglow luminescence properties. At last, the proof-of concept applications are demonstrated for *in vivo* hypoxia imaging and *in vivo* imaging of metastatic tumors.

2. Results and Discussion

The PPVs were synthesized according to Figure 1a. Monomer 1,4-dibromo-2,5-bis((2-ethylhexyl)oxy)benzene was synthesized by 2,5-dibromohydroquinone and 3-

(bromomethyl)heptane in the presence of potassium carbonate (**Figure S1, Supporting Information**). 1,4-Dibromo-2,5-bis((2-ethylhexyl)oxy)benzene was then copolymerized with trans-1,2-bis (tributylstannyl) ethene and 7,18-dibromo-5,10,15,20-tetraphenylporphyrin (TPP-Br) at different feeding ratio to yield PPV, PPV-$TPP_{2.5\%}$ and PPV-$TPP_{5\%}$ *via* Pd-catalyzed Stille coupling reaction (**Figure 1a**). As shown in the ^{1}H NMR of PPV-TPPs (Figure S2-S4, Supporting Information), the characteristic resonance peaks of TPP were found at 8.8, 8.2 and 7.8 ppm and the peaks of PPV backbone were found at 7.5, 7.2-7.1, 4.08-3.86, 3.40, 1.89, 1.30, 0.90-0.88 ppm, indicating the success of incorporation of TPP into PPV-TPPs. The molecular weight and polydispersity (PDI) of PPV-TPPs were further characterized by Gel permeation chromatography (GPC), and the molecular weights of PPV polymers ranged from 8900 to 13000 g/moL (Table S1, Supporting Information). All the polymers had good solubility in tetrahydrofuran (THF), which facilitated the nanoprecipitation process used for the preparation of water-soluble nanoparticles.

Nanoprecipitation was used to transform PPV, PPV-$TPP_{2.5\%}$ and PPV-$TPP_{5\%}$ into the water-soluble nanoparticles (named as SPN0, SPN2.5 and SPN5, respectively) in the presence of an amphiphilic triblock copolymer (PEG-b-PPG-b-PEG) (Figure 1b). Dynamic light scattering (DLS) showed that the average hydrodynamic diameters of SPN0, SPN2.5 and SPN5 were similar, ranging from 25 to 30 nm (Figure 1c and Figure S6 Supporting Information). Taking SPN2.5 as the example, transmission electron microscopy (TEM) showed its uniform spherical morphology with an average diameter of ~ 25 nm (Figure 1d), nearly identical to the DLS data. No precipitation or obvious change in size was observed for SPN2.5 after storage in phosphate buffer saline (PBS) (pH = 7.4) or fetal bovine serum (FBS) for 20 days (Figure S7, Supporting Information). In addition, SPN2.5 was non-cytotoxic to 4T1 cells as confirmed by 3-(4,5-dimethyl-thiazol-2-yl)-5-(3-carboxymethoxyphenyl)-2-(4-sulfophenyl)-2H-tetrazolium

(MTS) assay (Figure 1e). These results indicated that these SPNs should be suitable for biological applications.

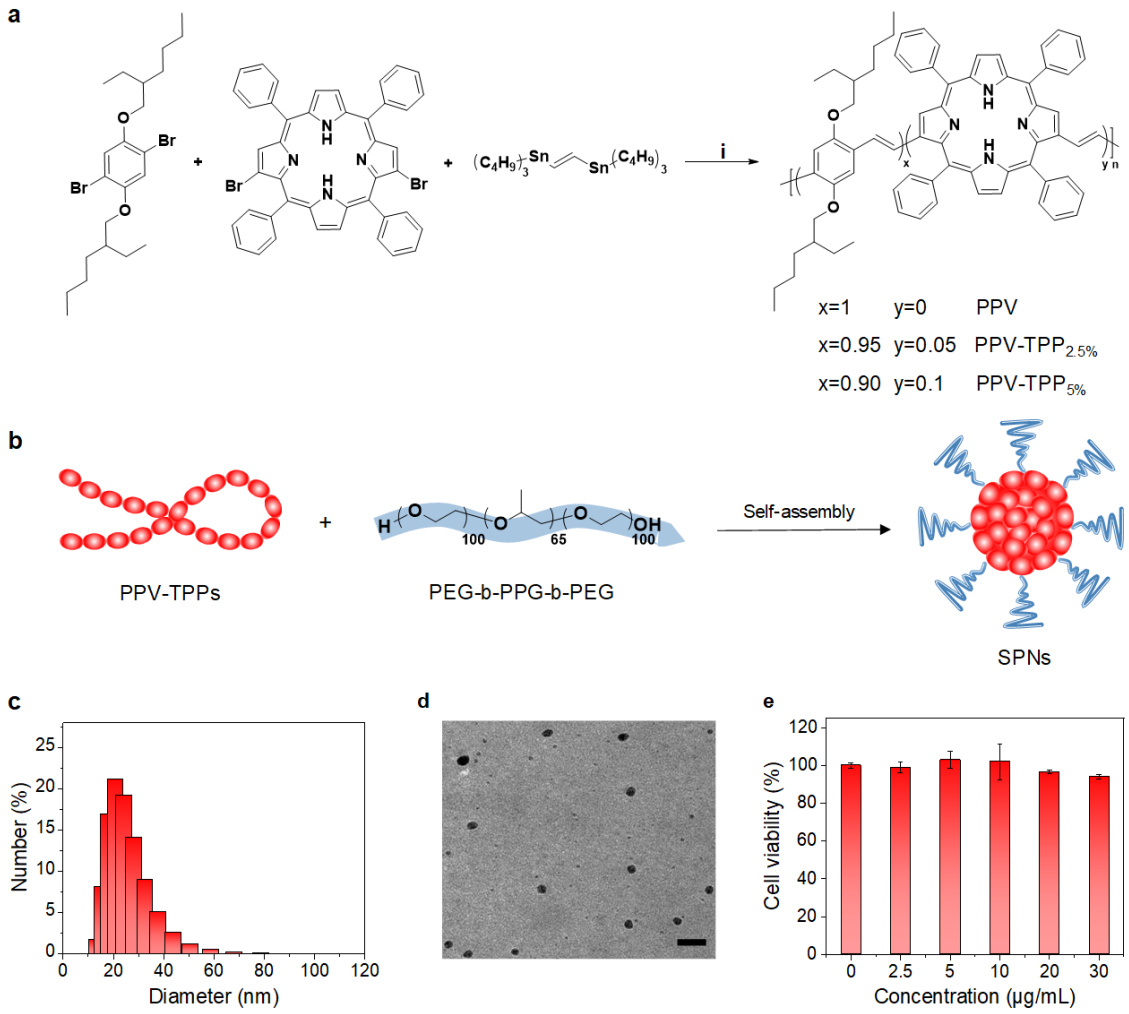

Figure 1. Synthesis and characterization of SPNs. (a) Synthesis route of PPV, PPV-TPP$_{2.5\%}$ and PPV-TPP$_{5\%}$. Reagents and conditions: i) tris(dibenzylideneacetone)dipalladium(0) [Pd2(dba)3], tri(p-tolyl)phosphine (TP), chlorobenzene, 100 ºC, 24 h. (b) Schematic illustration of the preparation of SPNs. (c) DLS of SPN2.5 in 1×PBS buffer (pH = 7.4). The PDI of SPN2.5 is 0.356. (d) TEM images of SPN2.5. The scale bar represents 100 nm. (e) Cell viability of 4T1 cells after incubation with SPN2.5 solutions at various concentrations. Error bars represent standard deviations of three separate measurements (n = 3).

The optical properties of SPNs were tested in PBS solution (pH = 7.4). The ultraviolet (UV) Vis spectra showed that all the SPNs had similar maximum absorption ranging from 430 to 450 nm (**Figure 2a**). Such an absorption band was assigned to the PPV segment as confirmed

by the absorption spectra of the polymers in THF (Figure S5a, Supporting Information). With increasing the doping amount of TPP, a new absorption band of SPNs ranging from 600 to 700 nm appeared and gradually increased, verifying the incorporation of TPP into the backbone of PPV. The fluorescence of TPP-free nanoparticle (SPN0) had a visible emission with the maximum peak at 580 nm assigned to the PPV segment. With increased amount of TPP, the fluorescence at 580 nm decreased accompanied with increased NIR emission of TPP ranging from 650 to 750 nm (Figure 2b and 2d), and the saturation occurred at the doping amount of 2.5% (SPN2.5). Such a spectral change confirmed the occurrence of fluorescence resonance energy transfer (FRET) from PPV segments to TPP, which was consistent with the good spectral overlap between the absorption of TPP and the emission of PPV from 500 to 700 nm (Figure S7b, Supporting Information). However, as compared with SPN2.5, SPN5 showed decreased emission of TPP from 650 to 750 nm. The fluorescence images of SPNs at 720 nm acquired by IVIS also confirmed this spectral change (Figure 2d). To understand this phenomenon, the PPV-free nanoparticles were prepared via nanoprecipitation of TPP and PEG-b-PPG-b-PEG. Although the concentration of TPP was doubled (Figure S8 in Supporting Information), the fluorescence decreased with increasing the doping concentration of TPP from 1 to 2%. Thus, the decreased fluorescence for SPN5 relative to SPN2.5 should be similarly attributed to the fluorescence self-quenching of TPP induced by its high local concentration, which was widely reported in the previous studies.[27] The quantification data showed that the absolute total fluorescence intensity of SPN0 was ~ 1.83 and ~ 3.67-fold higher than that of SPN2.5 and SPN5, respectively (Figure 2e). The decreased total fluorescence intensity should be attributed to the energy loss caused by FRET and the fluorescence self-quenching of TPP within SPN2.5 and SPN5.

The afterglow spectra and images of SPNs were collected after light irradiation under bioluminescence modes (without real-time excitation). The spectral profiles of afterglow were

similarly to the fluorescence spectra (Figure 2c). However, with increasing doping of TPP, the absolute total afterglow intensity increased for both SPN2.5 and SPN5 relative to SPN0 (Figures 2d&2e), which were different from the absolute total fluorescence intensity (decreased with increasing doping of TPP). Moreover, the highest absolute afterglow intensity was observed for SPN2.5 rather than SPN5 (Figure 2e), which were ~ 6.12 and ~ 2.14-fold higher than that of SPN0 and SPN5, respectively. Such a difference in the absolute intensity between afterglow and fluorescence should be associated with their different luminescent mechanisms. As tested by $^1O_2$ sensor green (SOSG), the fluorescence intensities of SOSG at 528 nm in the presence of SPN0, SPN2.5 and SPN5 increased by 6.44-, 7.78- and 9.96-fold, respectively, after light irradiation for 4 min (Figure S9, Supporting Information). This proved that with increased doping amount of TPP, more $^1O_2$ was generated during light irradiation, and thus more PPV-dioxetane intermediates were produced, leading to the amplified afterglow for SPN2.5 and SPN5 relative to SPN0. However, due to the self-quenching of TPP, SPN5 had lower absolute afterglow intensity than SPN2.5. These data confirmed that incorporation of TPP into the backbone of PPV could amplify and red-shift its afterglow signal.

With the brightest afterglow intensity among all the SPNs, SPN2.5 was chosen for *in vivo* imaging experiments. It was noted that the afterglow intensity of SPN2.5 could be increased by 1.90-fold when measured in O_2-saturated condition, while decreased by 4.06-fold when measured in N_2-saturated condition (Figure S10, Supporting Information); the addition of a $^1O_2$ scavenger (NaN_3) could reduce the afterglow intensity by 1.58-fold. In addition, the afterglow luminescence half-life of SPN2.5 was 5 min at room temperature (Figure 2f), long enough for imaging acquisition.

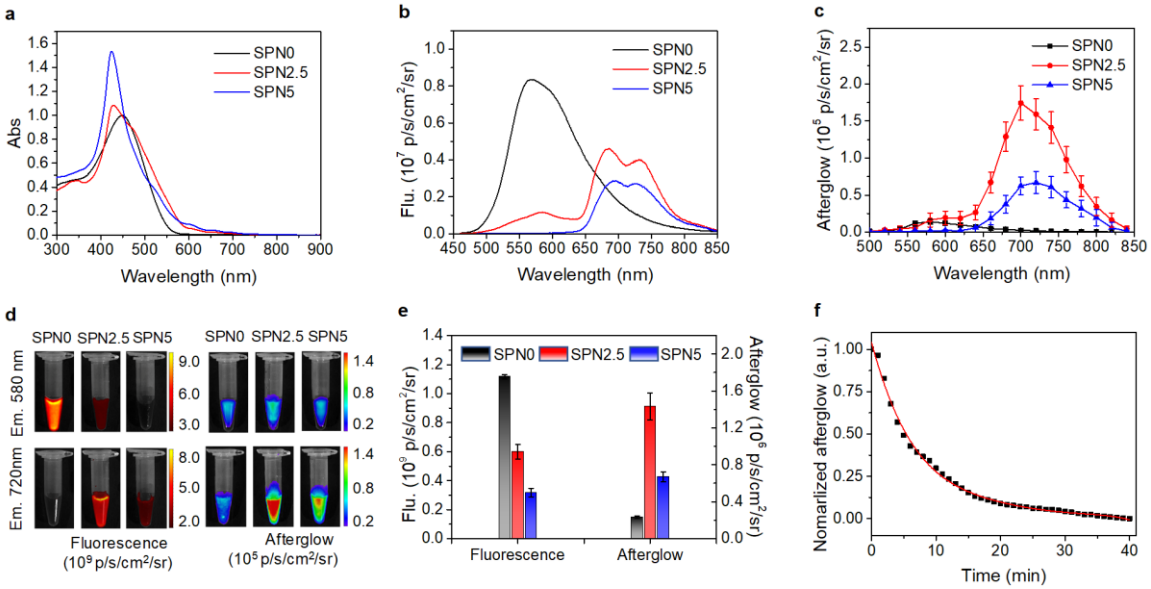

Figure 2. Optical characterization of SPNs. (a) UV-visible absorption spectra of SPNs. The concentration of PPV component for all SPNs were 30 μg/mL in 1× PBS (pH = 7.4). (b) Fluorescence spectra of SPNs. The concentration of PPV component of all SPNs were 100 μg/mL in 1× PBS (pH = 7.4). (c) Afterglow luminescence spectra of SPNs (100 μg/mL). SPNs solutions were pre-irradiated for 1 min by white light before the collection of afterglow luminescence signal. The error bars represent the standard deviations of three separate measurements. (d) Fluorescence and afterglow luminescence images of SPNs in 1× PBS (pH = 7.4) upon excitation at 430 nm with different emission at 580 nm (up) and 720 nm (bottom). The afterglow images were acquired for 30 s after the pre-irradiation of SPNs under white light at a power density of 1 W/cm^2 for 1 min. (e) Quantification of absolute fluorescence and afterglow intensities of SPNs. The error bars represent the standard deviations of three separate measurements. (f) Normalized decay of afterglow luminescence of SPNs (100 μg/mL) at room temperature. SPNs solutions were pre-irradiated for 1 min by white light before the collection of afterglow luminescence signal. The light power used in the experiments was 1 W/cm^2.

Most tumor cells are in the hypoxic environment resulting from their rapid oxygen consuming for vasculature growth and cell proliferation [28]. Because tumor hypoxia is associated with increased risk of invasion and metastasis, imaging of tumor hypoxia can be helpful for diagnosis and treatment of cancer. Because afterglow was sensitive to oxygen (Figure S8, Supporting Information), SPN2.5 was then utilized to differentiate hypoxia and normoxia *in vivo*. The SPN2.5 solution was deoxygenated and then locally injected into tumor

or under skin (**Figure 3a**). The fluorescence images of the mice were acquired at 720 nm upon excitation at 500 nm, while the afterglow luminescence images were obtained with a 30 s acquisition time with an open filter after pre-irradiated with white light for 1 min (Figure 3b). Signal quantification clearly showed that the afterglow intensity of locally injected skin was 3.56-fold higher than that of tumor while the fluorescence intensities between skin and tumor were almost the same (Figure 3c). The lower afterglow signal in tumor was attributed to the hypoxia environment of tumor, which had a low oxygen level that reduced the generation of $^1O_2$ and in turn the afterglow intensity of SPN2.5. These data indicated that afterglow luminescence of SPN2.5 could be potentially used to distinguish hypoxia from normoxia environment in living mice.

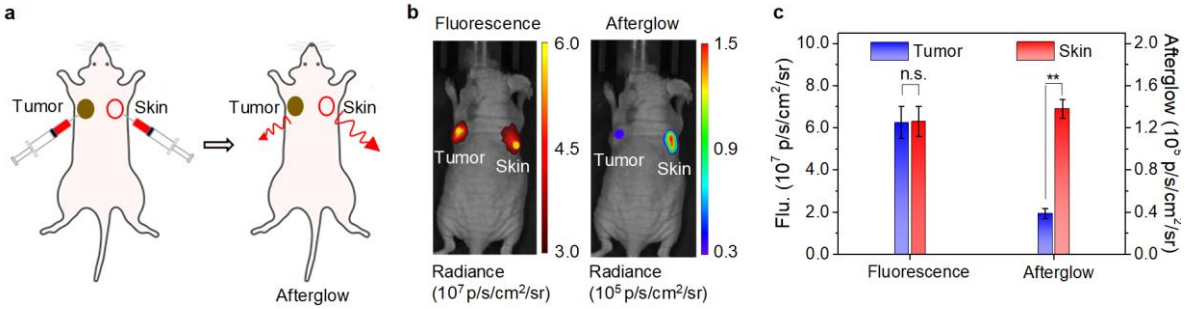

Figure 3. *In vivo* imaging of tumor hypoxia. (a) Schematic illustration of afterglow imaging of hypoxia and normoxia in a living mouse. SPN2.5 was purged with N_2 to remove oxygen before injection. (b) Fluorescence and afterglow luminescence images of tumor and skin after local injection of SPN2.5 (100 μg/mL, 50 μL). (c) Fluorescence and afterglow intensities of tumor and skin after local injection of SPN2.5 (100 μg/mL, 50 μL). Error bars represent standard deviations of three separate measurements (n = 3). n.s.: not significant, ** statistically significant difference ($p < 0.01$, n = 3).

To test the ability of SPN2.5 in imaging of metastatic tumor tissues, the peritoneal metastatic tumor mouse model was established by injecting 4T1 cell suspension (200 μL, 4×10^5) intraperitoneally into nude mice, and the healthy mice without injection of 4T1 cells was used as the control. The mice in both groups were injected with SPN2.5 through tail vein 4 d after the injection of cancer cells. Fluorescence and afterglow images were acquired at different

time points post-injection of SPN2.5. Obvious afterglow signal from the liver (indicated by black circle) were observed for both groups at t = 20 min post-injection, while fluorescence signal of liver could only be detected after 1 h (**Figure 4a**). This reflected the higher tissue penetration of afterglow imaging relative to of fluorescence imaging. The afterglow intensity of lower quadrant region (indicted by white frame) gradually increased for 4T1 tumor-bearing mice (Figures 4a & Figure 4c); in contrast, no obvious afterglow signal at the same region could be detected for the control group. At t = 4 h post-injection, the afterglow signal in the lower quadrant region of 4T1 tumor-bearing mice was 27.6-times higher than background, while it was similarly to the background for the control mice. At this time point, skin and peritoneum of mice were removed and the lower quadrant region of mice were imaged by both afterglow and fluorescence. Due to the high sensitivity of afterglow, strong afterglow spots were detected on the intestines of T1 tumor-bearing mice, while only autofluorescence was detected in the abdominal cavity and no afterglow signal was observed for the control mice (Figure 4b). Histological examinations further confirmed the presence of tiny and naked eye barely detectable metastatic tumors on the surface of intestine (Figure 4d). Moreover, the fluorescence confocal imaging of tumor slices indicated that SPN2.5 had a good accumulation at the tumor site (Figure 4e). These data proved that the afterglow signals on the intestine site of 4T1 tumor-bearing mice came from the metastatic tumor tissues and indicated that SPN2.5 could be used as a potential afterglow imaging agent for *in vivo* detection of metastatic tumors.

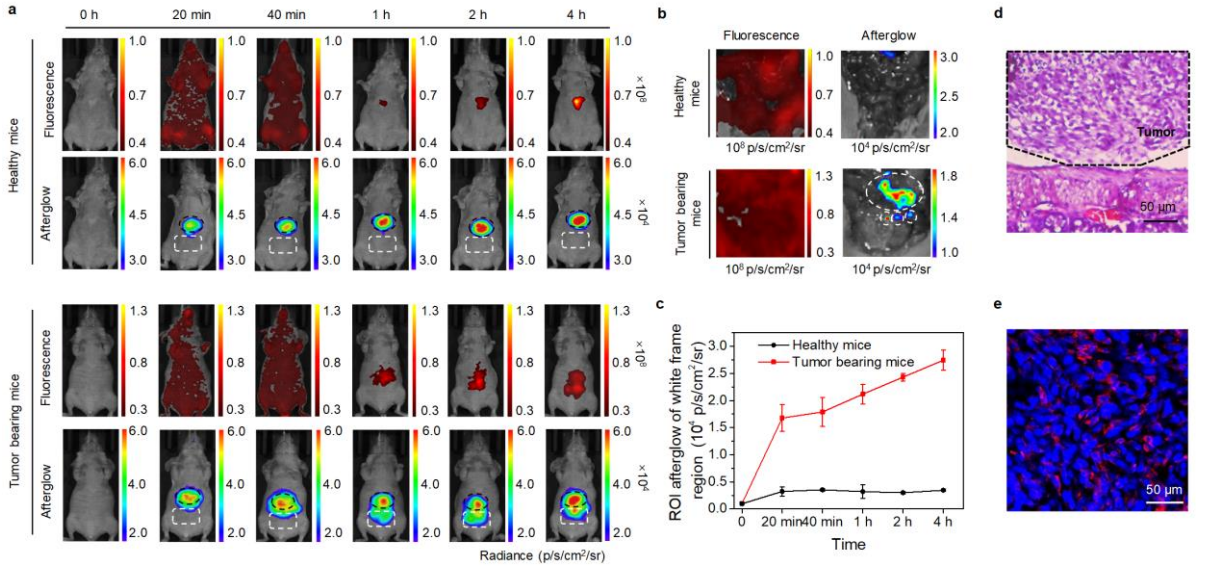

Figure 4. *In vivo* peritoneal metastatic tumor imaging. (a) Fluorescence and afterglow luminescence images of healthy mice (up) and peritoneal metastatic tumor bearing mice (bottom) at different time points after intravenous injection of SPN2.5 (400 μg/mL, 200 μL). The liver site is marked by black circle. The lower quadrant region is marked by white frame. (b) Fluorescence and afterglow luminescence images of mice with skin removed to expose the abdominal cavity at 4 h post-injection of SPN2.5. The lower quadrant region is marked by white circles. (c) Afterglow luminescence intensities of the lower quadrant region (white frame) for SPN2.5-injected mice as a function of post-injection time in Figure 4a. Error bars represent standard deviations of three separate measurements (n = 3). (d) H&E stained slices and (e) confocal images of slices of peritoneal metastatic tumor obtained from SPN2.5-injected mice. The tumor regions are marked by black frames. For the fluorescence images, SPN2.5 was indicated as red color. The nuclei were stained by 4',6-diamidino-2-phenylindole (DAPI) indicated as blue color.

3. Conclusion

We have synthesized a series of photosensitizer-incorporated PPVs and transformed them into afterglow nanoagents for *in vivo* imaging. With the help of FRET and promoted $^1O_2$ generation, SPN2.5 showed the NIR afterglow with the maximum at 720 nm, and amplified afterglow intensity that was 6.12-fold brighter than the non-doped nanoparticles (SPN0). The oxygen-sensitive afterglow of SPN2.5 made it useful for *in vivo* imaging of tumor hypoxia,

showing 3.56-fold higher afterglow in skin than that in hypoxic tumor. In addition, the bright afterglow of SPN2.5 was used to detect tiny peritoneal metastatic tumor tissues in living mice through systemic administration. Due to the high sensitivity of afterglow imaging, metastatic tumor tissues could be delineated by afterglow spots on the intestines of SPN2.5 injected mice, which was not possible for fluorescence imaging. Thus, this study introduces a new generation of organic afterglow nanoagents with self-amplified signal for light-excitation-free *in vivo* imaging.

Experimental Section

Chemicals and Other Materials. All chemicals were purchased from Sigma-Aldrich (St. Louis, MO, USA) unless otherwise stated. Dialysis membrane with 3 kDa MWCO was purchased from Spectrum Labs.

Characterization. Transmission electron microscopy (TEM) images were obtained on a JEM 1400 transmission electron microscope with an accelerating voltage from 40 to 120 kV. Dynamic light scattering (DLS) and zeta potential were obtained on the Malvern Nano-ZS Particle Size. Ultraviolet (UV)-Vis spectra were recorded on a Shimadzu UV-2450 spectrophotometer. Fluorescence measurements were carried out on a Fluorolog 3 times correlated single photon counting (TCSPC) spectrofluorometer. Gel permeation chromatography (GPC) was conducted by a Shimadzu LC-VP system with polystyrenes as the standard and high-performance liquid chromatography (HPLC) grade THF as the eluent. Nuclear Magnetic Resonance (NMR) spectroscopy was recorded on a BRUKER Avance 300 NMR (1H, 300MHz) system with CDCl3 or D2O as the solvent. The spectrum was internally referenced to the Tetramethylsilane signal at 0 ppm. Afterglow signals and images were collected and obtained with the IVIS Spectrum imaging system under bioluminescence (without excitation) mode.

Synthesis of Monomer 1,4-Dibromo-2,5-bis((2-ethylhexyl)oxy)benzene. 2,5-Dibromohydroquinone (500 mg, 1.87 mmol), potassium carbonate (780 mg, 5.61 mmol) and dimethylformamide (DMF) were added to a 50 mL round-bottomed flask, followed by 3-(bromomethyl)heptane (0.8 mL, 4.58 mmol) addition. The mixture was carried out at 80 °C for 12 hours. The product was cooled to room temperature and extracted with dichloromethane (DCM). The organic layer was washed with water/ brine and dried over anhydrous sodium sulfate. The solvent was removed under vacuum, and the crude was purified via column chromatography over silica/hexane, yielding 1,4-dibromo-2,5-bis((2-ethylhexyl)oxy)benzene (697.5 mg, 76.3% yield) as a pale viscous oil. ^{1}H NMR (300 MHz, $CDCl_3$) δ 7.08 (s, 2H), 3.82 (d, J = 5.6 Hz, 4H), 1.73 (dd, J = 12.1, 6.0 Hz, 2H), 1.61 – 1.20 (m, 16H), 0.93 (t, J = 7.5 Hz, 12H).

General Procedure for Synthesis of PPV-TPP. 1,4-Dibromo-2,5-bis((2-ethylhexyl)oxy)benzene, 7,18-dibromo-5,10,15,20-tetraphenylporphyrin, trans-1,2-Bis(tributylstannyl)ethene, tris(dibenzylideneacetone)dipalladium(0) and tri(p-tolyl)phosphine were added to a 50 mL Schlenk tube, followed by Chlorobenzene addition via syringe (degassed). The tube was charged with argon through freeze–pump-thaw cycles for three times. The reaction was carried out at 100 °C under vigorous stirring for 24 h. The mixture was cooled to room temperature and the solvent was removed under vacuum. The crude product was poured into methanol and the obtained brown solid was washed with methanol for three times.

PPV: ^{1}H NMR (300 MHz, $CDCl_3$) δ 7.46 (s, 1H), 7.12 (d, J = 21.9 Hz, 2H), 3.95 (t, J = 29.7 Hz, 4H), 3.40 (s, 1H), 1.89 (s, 2H), 1.30 (d, J = 26.2 Hz, 3H), 0.90 (s, 4H).

PPV-$TPP_{2.5\%}$: ^{1}H NMR (300 MHz, $CDCl_3$) δ 8.22 (s, 1H), 7.77 (s, 2H), 7.42 (d, J = 25.4 Hz, 4H), 7.12 (d, J = 18.6 Hz, 4H), 4.03 (d, J = 30.0 Hz, 7H), 3.43 (d, J = 6.7 Hz, 8H), 1.90 (s, 14H), 1.26 (s, 6H), 0.96 – 0.69 (m, 5H).

PPV-TPP$_{5\%}$: ^{1}H NMR (300 MHz, $CDCl_3$) δ 8.21 (s, 1H), 7.77 (s, 1H), 7.49 (s, 2H), 7.23 – 6.97 (m, 2H), 3.95 (t, J = 31.0 Hz, 4H), 3.28 (s, 1H), 1.96 (d, J = 47.6 Hz, 2H), 1.62 (d, J = 34.3 Hz, 6H), 1.27 (t, J = 18.3 Hz, 5H), 1.08 – 0.67 (m, 5H).

Preparation of SPNs. PPV-TPP (1 mg) was dissolved in 1 mL of THF. Then 0.25 mL of PPV-TPP THF solution and PEG-b-PPG-b-PEG (20 mg) were added into 0.75 mL of THF. The obtained solution was rapidly injected into a mixture of DI water (9 mL) and THF (1 mL) under continuous sonication. Then THF was removed by a gentle nitrogen flow. The resulting solution was purified by filtration through a 0.22 μm polyvinylidene fluoride syringe driven filter (Millipore). The obtained nanoparticles solutions were concentrated through ultrafiltration and then diluted by 1 × PBS (pH = 7.4) to prepare solutions of different concentrations.

Cell Culture and Cytotoxicity Assay. The *in vitro* cytotoxicity was measured using [3-(4,5-dimethylthiazol-2-yl)-5- (3-carboxymethoxyphenyl)-2-(4-sulfophenyl)-2H-tetrazolium (MTS) viability assay in 4T1 cell line. The 4T1 cells were cultured in Dulbecco's Modified Eagle Medium (DMEM) containing 10% fetal bovine serum in a humidified environment containing 5% CO2 and 95% air at 37 °C. 4T1 cells were seeded in 96-well plates (Costar, IL, U.S.A.) at an intensity of 3×104 cells/mL. After 24 h incubation, the medium was replaced by fresh medium containing SPNs suspensions at different concentrations (0, 2.5, 5, 10, 20, 30 μg/mL) and the cells were then incubated for 24 h. After the designated time intervals, MTS reagent was added into cell culture medium in 1 to 10 volume ratios for cell incubation. UV measurement (490 nm) was taken after 3 h in an incubator and normalized against untreated samples to the cell viability.

In Vitro Fluorescence and Afterglow Measurement. Fluorescence and afterglow luminescence images, fluorescence and afterglow spectra were acquired by using an IVIS Spectrum imaging system. Fluorescence images were acquired for 0.1 s with excitation at 465 ± 10 nm or 430 ± 10 nm, and emission at 520 ± 20 nm or 720 ± 20 nm. For afterglow

luminescence imaging, samples were pre-irradiated by white light for 1 min at a power density of 1 W/cm^2.

Animals and Tumor Mouse Model. All animal experiments were performed in compliance with the Guidelines established by the Institutional Animal Care and Use Committee (IACUC), Sing Health. To establish tumor-bearing mouse model, 4T1 cell suspension (200 μL, 1 × 10^6) was injected subcutaneously in the left shoulder of the nude mice. Tumors were grown for approximately 7 days before imaging experiments. To establish the peritoneal metastases mouse model, 4T1 cell suspension (200 μL, 4 × 10^5) was injected intraperitoneally into nude mice. Tumors were grown for approximately 4 days before imaging experiments.

In Vivo Imaging for Differentiating Hypoxia and Normoxia Environment. After anesthesia, pre-implanting tumor in the left shoulders of nude mice (n=2) were injected in situ with 50 μL of SPN2.5 (100 μg/mL, oxygen was removed via purging the solution with nitrogen). The same SPN2.5 solution was injected subcutaneously in the right shoulder of these mice. The fluorescence images of the mice were acquired at 720 nm upon excitation at 500 nm with the IVIS Spectrum imaging system. After pre-irradiated with white light for 1 min, the afterglow luminescence images of the mice were obtained with a 30s acquisition time under the IVIS Spectrum imaging system bioluminescence (open filter) mode.

Peritoneal Metastatic Tumor Imaging. The healthy mice were injected intravenously with 200 μL of SPN2.5 (400 μg/mL). The mice bearing the 4T1 intraperitoneal metastases were injected intravenously with 200 μL of SPN2.5 (400 μg/mL). At different post injection time point (0 h, 20 min, 40 min, 1 h, 2 h, 4 h), the fluorescence images of the mice were acquired at 720 nm upon excitation at 500 nm, while the afterglow luminescence images were then acquired with a 30s acquisition time with an open filter after irradiated with white light for 1 min. The mice were euthanized at 4 h post-injection, and the fluorescence and afterglow luminescence images of the organs and tumors with skin and peritoneum removed were acquired by applying

the same method described above. Fluorescence and afterglow luminescence images were analyzed by ROI analysis using the Living Image 4.0 Software.

Histological Analysis. To confirm the peritoneal metastatic tumor cells, the mice were euthanized and the tumors (tissues) were extracted and fixed in 4% paraformaldehyde. The tumors (tissues) were then embedded in paraffin S15 and cut into sections with a thickness of 10 μm for hematoxylin and eosin (H&E) staining according to the standard protocols. Images of stained slices were captured by a Nikon ECLIPSE 80i microscope (Nikon Corporation, Towa Optics, New Delhi, India).

Statistical Analysis. The fluorescence and afterglow luminescence images were quantified with ROI analysis using Living Image 4.0 Software. Results are expressed as the mean ± SD deviation unless otherwise stated. Statistical comparisons between two groups were determined by student t-test. For all tests, $p < 0.05$ was considered as statistically significant. All statistical calculations were performed using GraphPad Prism v.6 (GraphPad Software Inc., CA, USA).

Supporting Information

Supporting Information is available from the Wiley Online Library or from the author.

Acknowledgements

K.P. thanks Nanyang Technological University start-up grant (NTU-SUG: M4081627.120), Academic Research Fund Tier 1 from Singapore Ministry of Education (RG133/15: M4011559 and 2015-T1-002-091) and Academic Research Fund Tier 2 from Ministry of Education in Singapore (MOE2016-T2-1-098) for the financial support.

Received: ((will be filled in by the editorial staff))
Revised: ((will be filled in by the editorial staff))
Published online: ((will be filled in by the editorial staff))

References

[1] a) S. Valastyan, R. A. Weinberg, *Cell.* **2011**, *147*, 275; b) Q. J. He, S. R. Guo, Z. Y. Qian, X. Y. Chen, *Chem. Soc. Rev.* **2015**, *44*, 6258; c) P. S. Steeg, *Nat. Med.* **2006**, *12*, 895; d) C. L. Chaffer, R. A. Weinberg, *Science.* **2011**, *331*, 1559.

[2] R. M. Kwee, T. C. Kwee, *Gastric Cancer.* **2009**, *12*, 6.

[3] R. Qiao, R. Zhu, M. Gao, *Curr Pharm Des.* **2015**, *21*, 6260.

[4] P. Mi, D. Kokuryo, H. Cabral, H. L. Wu, Y. Terada, T. Saga, I. Aoki, N. Nishiyama, K. Kataoka, *Nat. Nanotechnol.* **2016**, *11*, 724.

[5] D. Entenberg, S. Voiculescu, P. Guo, L. Borriello, Y. Wang, G. S. Karagiannis, J. Jones, F. Baccay, M. Oktay, J. Condeelis, *Nat. Methods* **2018**, *15*, 73.

[6] a) D. Asanuma, M. Sakabe, M. Kamiya, K. Yamamoto, J. Hiratake, M. Ogawa, N. Kosaka, P. L. Choyke, T. Nagano, H. Kobayashi, Y. Urano, *Nat. Commun.* **2015**, *6*, 6463; b) S. Santagata, L. Portella, M. Napolitano, A. Greco, C. D'Alterio, M. V. Barone, A. Luciano, M. Gramanzini, L. Auletta, C. Arra, A. Zannetti, S. Scala, *Sci Rep.* **2017**, *7*, 2554.

[7] B. Ballou, L. A. Ernst, S. Andreko, T. Harper, J. A. J. Fitzpatrick, A. S. Waggoner, M. P. Bruchez, *Bioconjugate Chem.* **2007**, *18*, 389.

[8] X. Yu, D. Gao, L. Gao, J. Lai, C. Zhang, Y. Zhao, L. Zhong, B. Jia, F. Wang, X. Chen, Z. Liu, *ACS Nano* **2017**, *11*, 10147.

[9] a) K. Lee, H. Lee, K. H. Bae, T. G. Park, *Biomaterials.* **2010**, *31*, 6530; b) Y. Li, J. Tang, D. X. Pan, L. D. Sun, C. Chen, Y. Liu, Y. F. Wang, S. Shi, C. H. Yan, *ACS Nano* **2016**, *10*, 2766.

[10] a) X. Zheng, H. Tang, C. Xie, J. Zhang, W. Wu, X. Jiang, *Angew. Chem. Int. Ed.* **2015**, *54*, 8094; b) A. H. Colby, S. M. Berry, A. M. Moran, K. A. Pasion, R. Liu, Y. L. Colson, N. Ruiz-Opazo, M. W. Grinstaff, V. L. Herrera, *ACS Nano* **2017**, *11*, 1466.

[11] A. M. Smith, M. C. Mancini, S. Nie, *Nat. Nanotechnol.* **2009**, *4*, 710.

[12] Q. le Masne de Chermont, C. Chaneac, J. Seguin, F. Pelle, S. Maitrejean, J. P. Jolivet, D. Gourier, M. Bessodes, D. Scherman, *Proc. Natl. Acad. Sci. U S A.* **2007**, *104*, 9266.

[13] a) A. Abdukayum, J. T. Chen, Q. Zhao, X. P. Yan, *J. Am. Chem. Soc.* **2013**, *135*, 14125; b) F. Liu, W. Yan, Y. J. Chuang, Z. Zhen, J. Xie, Z. Pan, *Sci Rep.* **2013**, *3*, 1554; c) J. Shi, X. Sun, J. Li, H. Man, J. Shen, Y. Yu, H. Zhang, *Biomaterials* **2015**, *37*, 260.

[14] T. Maldiney, A. Bessiere, J. Seguin, E. Teston, S. K. Sharma, B. Viana, A. J. Bos, P. Dorenbos, M. Bessodes, D. Gourier, D. Scherman, C. Richard, *Nat. Mater.* **2014**, *13*, 418.

[15] T. Maldiney, M. U. Kaikkonen, J. Seguin, Q. L. de Chermont, M. Bessodes, K. J. Airenne, S. Yla-Herttuala, D. Scherman, C. Richard, *Bioconjugate Chem.* **2012**, *23*, 472.

[16] J. Toppari, J. C. Larsen, P. Christiansen, A. Giwercman, P. Grandjean, L. J. Guillette, Jr., B. Jegou, T. K. Jensen, P. Jouannet, N. Keiding, H. Leffers, J. A. McLachlan, O. Meyer, J. Muller, E. Rajpert-De Meyts, T. Scheike, R. Sharpe, J. Sumpter, N. E. Skakkebaek, *Environ. Health Perspect.* **1996**, *104 Suppl 4*, 741.

[17] G. Hong, Y. Zou, A. L. Antaris, S. Diao, D. Wu, K. Cheng, X. Zhang, C. Chen, B. Liu, Y. He, J. Z. Wu, J. Yuan, B. Zhang, Z. Tao, C. Fukunaga, H. Dai, *Nat. Commun.* **2014**, *5*, 4206.

[18] a) X. Zhen, C. Zhang, C. Xie, Q. Miao, K. L. Lim, K. Pu, *ACS Nano* **2016**, *10*, 6400. b) X. Zhen, Y. Tao, Z. An, P. Chen, C. Xu, R. Chen, W. Huang, K. Pu, *Adv. Mater.* **2017**, *29*, 1606665.

[19] a) K. Pu, A. J. Shuhendler, J. V. Jokerst, J. Mei, S. S. Gambhir, Z. Bao, J. Rao, *Nat. Nanotechnol.* **2014**, *9*, 233; b) J. Li, S. J. Yoon, B. Y. Hsieh, W. Tai, M. O'Donnell, X. Gao, *Nano Lett.* **2015**, *15*, 8217; c) C. Xie, X. Zhen, Y. Lyu, K. Pu, *Adv. Mater.* **2017**, *29*, 1703693; d) C. Xie, X. Zhen, Q. Lei, R. Ni, K. Pu, *Adv. Funct. Mater.* **2017**, *27*, 1605397. e) Y. Jiang, P. K. Upputuri, C. Xie, Y. Lyu, L. Zhang, Q. Xiong, M. Pramanik, K. Pu, *Nano Lett.* **2017**, *17*, 4964. f) Y. Jiang, K. Pu, *Small.* **2017**, *13*, 1700710. f) S. Zhang, W. Guo, J. Wei, C. Li, X.J. Liang, M. Yin, *ACS Nano* **2017**, *11*, 3797.

[20] a) C. Zhu, L. Liu, Q. Yang, F. Lv, S. Wang, *Chem Rev.* **2012**, *112*, 4687; b) K. Chang, Y. Tang, X. Fang, S. Yin, H. Xu, C. Wu, *Biomacromolecules* **2016**, *17*, 2128. c) M. Lan, S. Zhao, Y. Xie, J. Zhao, L. Guo, G. Niu, Y. Li, H. Sun, H. Zhang, W. Liu, J. Zhang, P. Wang, W. Zhang, *ACS Appl. Mater. Interfaces.* **2017**, *9*, 14590. d) L. Guo, G. Niu, X. Zheng, J. Ge, W. Liu, Q. Jia, P. Zhang, H. Zhang, P. Wang, *Adv. Sci.* **2017**, *4*, 1700085. e) S. Zhao, G. Niu, F. Wu, L. Yan, H. Zhang, J. Zhao, L. Zeng, M. Lan, *J. Mater. Chem. B.* **2017**, *5*, 3651. f) S. Li, X. Wang, R. Hu, H. Chen, M. Li, J. Wang, Y. Wang, L. Liu, F. Lv, X.J. Liang, S. Wang, *Chem. Mater.* **2016**, *28*, 8669. g) F. F. An, W. Cao, X. J. Liang, *Adv. Healthcare Mater.* **2014**, *3*, 1162.

[21] a) Y. Lyu, Y. Fang, Q. Miao, X. Zhen, D. Ding, K. Pu, *ACS Nano* **2016**, *10*, 4472; b) H. Chen, J. Zhang, K. Chang, X. Men, X. Fang, L. Zhou, D. Li, D. Gao, S. Yin, X. Zhang, Z. Yuan, C. Wu, *Biomaterials* **2017**, *144*, 42. c) Y. Lyu, J. Zeng, Y. Jiang, X. Zhen, T. Wang, S. Qiu, X. Lou, M. Gao, K. Pu, *ACS Nano* **2018**, *12*, 1801. d) J. Li, J. Rao, K. Pu, *Biomaterials* **2018**, *155*, 217.

[22] a) C. Qian, J. Yu, Y. Chen, Q. Hu, X. Xiao, W. Sun, C. Wang, P. Feng, Q. D. Shen, Z. Gu, *Adv. Mater.* **2016**, *28*, 3313; b) J. Yu, C. Wu, X. Zhang, F. Ye, M. E. Gallina, Y. Rong, I. C. Wu, W. Sun, Y. H. Chan, D. T. Chiu, *Adv. Mater.* **2012**, *24*, 3498.

[23] A. J. Shuhendler, K. Pu, L. Cui, J. P. Uetrecht, J. Rao, *Nat. Biotechnol.* **2014**, *32*, 373.

[24] F. Lv, T. Qiu, L. Liu, J. Ying, S. Wang, *Small.* **2016**, *12*, 696.

[25] Y. Lyu, D. Cui, H. Sun, Y. Miao, H. Duan, K. Pu, *Angew. Chem. , Int. Ed.* **2017**, *56*, 9155.

[26] Y. Lyu, C. Xie, S. A. Chechetka, E. Miyako, K. Pu, *J. Am. Chem. Soc.* **2016**, *138*, 9049.

[27] a) M. Palner, K. Pu, S. Shao, J. Rao, *Angew. Chem. , Int. Ed.* **2015**, *54*, 11477; b) Q. Miao, C. Xie, X. Zhen, Y. Lyu, H. Duan, X. Liu, J. V. Jokerst, K. Pu, *Nat. Biotechnol.* **2017**, *35*, 1102.

[28] P. Carmeliet, R. K. Jain, *Nature.* **2011**, *473*, 298.

The table of contents entry:

Semiconducting photosensitizer-incorporated copolymers are synthesized and developed into the afterglow imaging nanoagents. Due to the presence of the photosensitizer within the backbone, such nanoagents have red-shifted near-infrared emission and amplified signal, permitting sensitive imaging of peritoneal metastatic tumors in living mice.

Keyword: Bioimaging

Author: D. Cui, Dr. C. Xie, Dr. J. Li, Y. Lyu, Prof. K. Pu

Title: Semiconducting Photosensitizer-incorporated Copolymers as Near-Infrared Afterglow Nanoagents for Tumor Imaging

ToC figure